The role of gelsolin domain 3 in familial amyloidosis (Finnish type)

Habiba Zorgati[a,b], Mårten Larsson[a,1], Weitong Ren[c], Adelene Y. L. Sim[d], Jan Gettemans[e], Jonathan M. Grimes[f,g], Wenfei Li[c,2], and Robert C. Robinson[a,h,i,2]

[a]Institute of Molecular and Cell Biology, Agency for Science, Technology and Research (A*STAR), 138673 Singapore, Singapore; [b]Department of Biochemistry, National University of Singapore, 117596 Singapore, Singapore; [c]National Laboratory of Solid State Microstructure, Department of Physics, Collaborative Innovation Center of Advanced Microstructures, Nanjing University, 210093 Nanjing, China; [d]Bioinformatics Institute, Agency for Science, Technology and Research (A*STAR), 138671 Singapore, Singapore; [e]Nanobody Lab, Department of Biomolecular Medicine, Faculty of Medicine and Health Sciences, Ghent University, B-9000 Ghent, Belgium; [f]Division of Structural Biology, Wellcome Trust Centre for Human Genetics, University of Oxford, Oxford OX3 7BN, United Kingdom; [g]Diamond Light Source Ltd., Didcot OX11 ODE, United Kingdom; [h]School of Biomolecular Science and Engineering, Vidyasirimedhi Institute of Science and Technology, 21210 Rayong, Thailand; and [i]Research Institute for Interdisciplinary Science, Okayama University, 700-8530 Okayama, Japan

Edited by Thomas D. Pollard, Yale University, New Haven, CT, and approved May 29, 2019 (received for review February 6, 2019)

In the disease familial amyloidosis, Finnish type (FAF), also known as AGel amyloidosis (AGel), the mechanism by which point mutations in the calcium-regulated actin-severing protein gelsolin lead to furin cleavage is not understood in the intact protein. Here, we provide a structural and biochemical characterization of the FAF variants. X-ray crystallography structures of the FAF mutant gelsolins demonstrate that the mutations do not significantly disrupt the calcium-free conformations of gelsolin. Small-angle X-ray–scattering (SAXS) studies indicate that the FAF calcium-binding site mutants are slower to activate, whereas G167R is as efficient as the wild type. Actin-regulating studies of the gelsolins at the furin cleavage pH (6.5) show that the mutant gelsolins are functional, suggesting that they also adopt relatively normal active conformations. Deletion of gelsolin domains leads to sensitization to furin cleavage, and nanobody-binding protects against furin cleavage. These data indicate instability in the second domain of gelsolin (G2), since loss or gain of G2-stabilizing interactions impacts the efficiency of cleavage by furin. To demonstrate this principle, we engineered non-FAF mutations in G3 that disrupt the G2-G3 interface in the calcium-activated structure. These mutants led to increased furin cleavage. We carried out molecular dynamics (MD) simulations on the FAF and non-FAF mutant G2-G3 fragments of gelsolin. All mutants showed an increase in the distance between the center of masses of the 2 domains (G2 and G3). Since G3 covers the furin cleavage site on G2 in calcium-activated gelsolin, this suggests that destabilization of this interface is a critical step in cleavage.

amyloid | gelsolin | FAF | AGel amyloidosis | structure

Familial amyloidosis, Finnish type (FAF), also known as AGel amyloidosis (AGel), is an autosomal-dominant and monogenic disease characterized by deposition of amyloid fibrils derived from the gelsolin protein in different organs and tissues. Symptoms include corneal lattice dystrophy, cranial neuropathy, skin elasticity problems, and renal complications (1–3). It was first described to be restricted to the Finnish population (4), but more recently, cases have been reported with known and novel mutations in individuals with genetic backgrounds from Africa, Asia, Europe, and South America (5–11). Most mutations known to cause gelsolin amyloidosis arise from a single-point mutation in exon 4 (G167R, N184K, and D187N/Y; mature plasma gelsolin numbering here and throughout the manuscript) (12–14). Recently, 3 new mutations were reported P432R, A551P, and one in exon 1, causing a frameshift in the gelsolin gene (Ala7fs) (11, 15–17).

The most common FAF mutation, D187N/Y (substitution of aspartic acid 187 to asparagine or tyrosine), occurs in the Ca^{2+} binding site of the second domain of gelsolin (G2), which prevents calcium binding to G2 (18–20). Therefore, disruption of the conformational changes of gelsolin upon calcium activation is thought to be aberrant, and G2 becomes unstable in the presence of these mutations (19, 21–23). Under these conditions, gelsolin becomes activated, but transformation from the closed inactive conformation to the open active conformation is likely to be less efficient (20). Another distinct gelsolin mutant involves the substitution of glycine to arginine at position 167 (G167R), a mutation that is not in a calcium-binding residue. This mutation has been proposed to cause domain-swapped aggregation (24). The various point mutations lead to partially misfolded protease-sensitive products (25), which are targeted when the proteins travel through the trans-Golgi network during secretion. There, the mutant gelsolins are cleaved by furin, and a C-terminal 68-kDa fragment (C68) is produced. This truncated fragment of gelsolin is then degraded by the membrane type 1 matrix metalloprotease on export outside the cell, giving rise to 8- and 5-kDa amyloidogenic fragments, which self-assemble (26). The frameshift mutation (Ala7fs) would not be expected to translate

Significance

In the disease familial amyloidosis, Finnish type (FAF) the mechanism by which point mutations in gelsolin domain 2 (G2) lead to furin cleavage is not understood for the intact protein. Here, we determine that FAF mutants adopt similar conformations to the wild-type protein. However, the mutations appear to affect the dynamics of domain:domain interactions. Thus, proper domain:domain interactions are needed to protect G2 from protease cleavage. We make mutations in the following domain (G3) that functionally mimic the FAF mutations in G2. We conclude that G2 is on the limits of stability, and perturbations that affect domain:domain stabilizing interactions tip the balance toward cleavage. These data explain how multiple FAF mutations give rise to amyloid formation.

Author contributions: H.Z., M.L., W.L., and R.C.R. designed research; H.Z., W.R., J.M.G., W.L., and R.C.R. performed research; M.L. and J.G. contributed new reagents/analytic tools; H.Z., A.Y.L.S., W.L., and R.C.R. analyzed data; and H.Z., M.L., W.L., and R.C.R. wrote the paper.

The authors declare no conflict of interest.

This article is a PNAS Direct Submission.

Data deposition: The atomic coordinates and structure factors have been deposited in the Protein Data Bank, http://www.wwpdb.org (PDB ID codes 6JCO, 6JEH, and 6JEG).

[1]Present address: Science for Life Laboratory, Department of Medical Biochemistry and Microbiology, Uppsala University, 751 23 Uppsala, Sweden.

[2]To whom correspondence may be addressed. Email: wfli@nju.eu.cn or br.okayama.u@gmail.com.

This article contains supporting information online at www.pnas.org/lookup/suppl/doi:10.1073/pnas.1902189116/-/DCSupplemental.

Published online June 26, 2019.

the region of gelsolin to form FAF fragments (11), thus any amyloids formed from the Ala7fs mutation likely have a distinct composition relative to the other FAF fibrils.

We previously investigated the inactive and active conformations of wild-type (WT) gelsolin (27). Here, we assess the impact of the FAF mutations on the gelsolin structure using X-ray crystallography, small-angle X-ray scattering (SAXS), biochemical assays, and furin cleavage assays. We find that these mutations disrupt the dynamics of domain:domain interactions with G2 and lead to sensitization to furin cleavage. By contrast, the allosteric binding of a nanobody to G2 protects against furin cleavage. Together, these data suggest that G2 is close to the limit of stability and that multiple modifications are capable of shifting the balance toward instability.

Results

To understand the structural basis of the breakdown of gelsolin in FAF, we crystallized and solved the calcium-free X-ray structures of the FAF mutant gelsolins G167R, D187N, and D187Y (28–30). These mutants crystallized in the wild-type crystallization conditions and formed crystals of the same space group and similar cell dimensions. Molecular replacement using the wild-type structure led to structures of the mutants that showed no gross conformational changes with respect to the wild-type structure (Fig. 1), characterized by RMSDs of 0.41–0.51 Å in comparison with the wild-type structure (Fig. 1*F*). The mainchain electron density around the mutation sites was well defined with reasonable density for the mutant sidechains (Fig. 1 *A*–*E*), indicating that the mutations do not induce large changes in the calcium-free gelsolin structure. Closer examination of the mutation conformations revealed differences in the bonding patterns of the mutant residues. Wild-type Asp187 is able to form a charge–charge interaction with Lys166 and 2 potential hydrogen bonds with Asn184 and Gln164, interactions that stabilize the G2 β-sheet (*SI Appendix*, Fig. S1). The D187N mutant loses the ability to form the charge–charge interaction but can form potential hydrogen bonds with Gln164, Lys166, and Asn184 (*SI Appendix*, Fig. S1*A*). D187Y is unable to form charge–charge interactions or hydrogen bonds with these residues (*SI Appendix*, Fig. S1*B*). By contrast, in the absence of a sidechain in wild-type Gly167, there is no loss of bonding pattern on mutation. However, the bulkier arginine residue approaches G3 (*SI Appendix*, Fig. S1*C*) and may pay a steric penalty. Furthermore, the sidechains around 167Arg show differences between the 2 copies in the asymmetric unit in this region. This indicates that loss of mainchain rotational freedom, in replacing glycine by arginine, and the difficulty in accommodating the bulkier residue, impacts on the mainchain conformation. The following residues, Arg168 and Arg169, form charge–charge interactions with Asp669 and Asp670, respectively, which are a major determinant of the G2:G6 interaction that locks the calcium-free

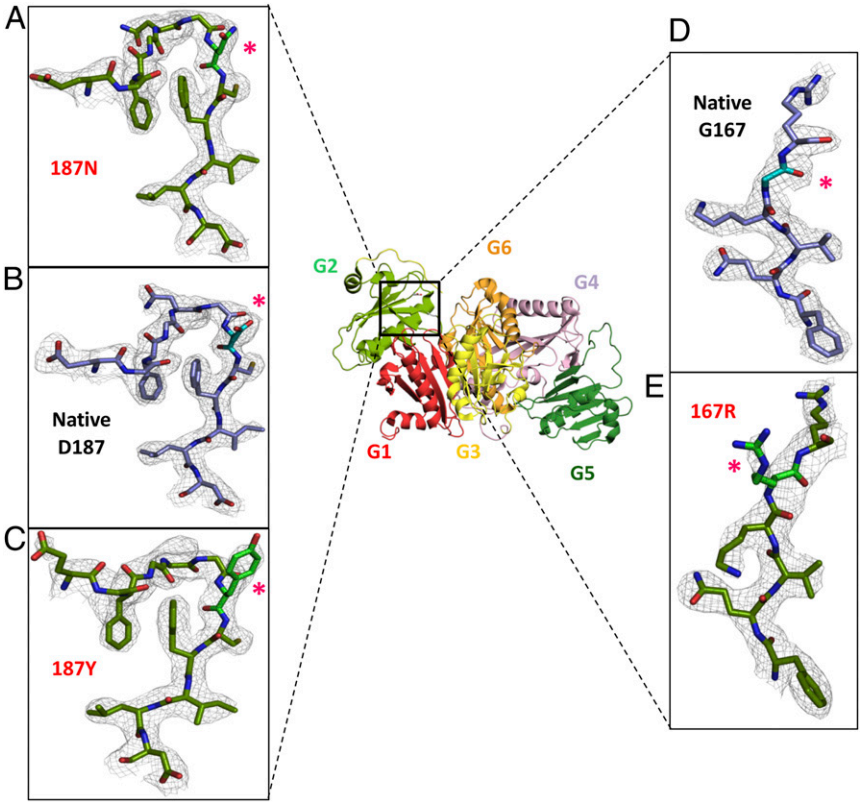

F

RMSD (Å / Residues)			
	187N	187Y	167R
WT	0.411/715	0.506/703	0.426/705

Fig. 1. Schematic representation of the structure of full-length gelsolin. Figure is colored with domain G1 in red, domain G2 in light green, domain G3 in yellow, domain G4 in purple, domain G5 in dark green, and domain G6 in orange (*Center*). The black square focuses on the FAF mutation region of domain G2. The 2Fo-Fc electron density map of the residues is shown as a gray grid comparing the 3 different mutants contoured at 1 σ, with (*A*) Asn187, (*B*) Native Asp187, (*C*) Tyr187, (*D*) Native Gly167, and (*E*) Arg167. Mutated residues are highlighted with a red star. (*F*) Comparison of the root-mean-square deviation values of the native gelsolin structure versus mutants.

structure (27). Any disruption to this interaction would be predicted to reduce the stability of the inactive conformation. Thus, the calcium-free structures display the normal gelsolin conformation, but may be dynamically less stable.

Next, we asked whether the mutant gelsolins are functional at pH 6.5, the pH of the trans-Golgi. In a pyrene–actin polymerization assay the mutant gelsolins, in the presence of calcium, were able to overcome the lag phase in actin polymerization, caused by the slow rate of the nucleation step of actin polymerization (Fig. 2*A*). This suggests that the mutants can be activated by calcium and bind to 2 actin monomers in an F-actin conformation that allows pointed end elongation. Furthermore, in an actin filament sedimentation assay the mutant gelsolins were able change the location of actin from the pellet to the supernatant on the addition of calcium (Fig. 2 *B*–*E*). This activity is consistent with the mutant gelsolins retaining their ability to undergo calcium-induced conformational changes to sever actin filaments. Thus, the active conformations of the FAF gelsolins appear to be normal by using biochemical activity as a proxy for assessing the ability to reach the active calcium-bound structure.

Since the D187N/Y mutations involve a type II calcium-binding site in G2 (31) we followed the global calcium-induced conformational changes in the gelsolins using time-resolved SAXS. For the wild-type protein, a clear conformational change was observed in the Kratky plots and in changing the radius of gyration (Rg) on adding calcium, and this change was close to completion at the first recordable time point (130 ms) measurement after the addition of calcium (Fig. 3 *A* and *E*). The calcium-binding site mutants showed delayed conformational changes. D187Y achieved the conformational change in the timeframe of the experiment (400 ms, Fig. 3 *B* and *E*), whereas D187N showed only partial conformational change within this timeframe (Fig. 3 *C* and *E*). Finally, the G167R mutant activated on the same timescale as the wild-type protein (Fig. 3 *D* and *E*). Thus, mutations to the G2 calcium-binding site result in lower efficiency in the calcium-induced conformational changes.

The stability of the calcium-free and calcium-bound structures was assessed using a thermal denaturation assay. In the absence of calcium, the G167R mutant was ∼4° less stable than the wild-type and the D187N/Y mutants (Fig. 3*F*), which had midpoints to their thermal denaturation transition profiles of ∼54 °C. The reduced G167R mutant stability may be attributed to the suboptimal interactions between G2 and G6, as discussed for the calcium-free crystal structure above. Addition of calcium increased the stability of all of the proteins, characterized by midpoints in their thermal denaturation profiles of ∼60 °C (Fig. 3*G*). This suggests that the final calcium-activated structures are similar for wild-type and mutant gelsolins. Taken together, these data indicate that the mutant proteins can adopt similar inactive and active structures to the wild-type proteins and that they are functional in regulating actin. However, the D187N/Y mutants show slightly delayed calcium activation, and the G167R mutant shows lower stability in its inactive form.

Next, we turned to a furin cleavage assay to understand how these minor differences translate into different biological outcomes. All 3 mutants, but not the wild type, showed cleavage by furin at pH 6.5, the approximate pH of the trans-Golgi (Fig. 4*A*). This effect was diminished in the presence of a nanobody (Nb11) that binds to G2 at a site that is distant from the furin cleavage site (Fig. 4*A*) (32). The furin cleavage became more robust under the same conditions when a fragment, comprised of domains 2 and 3 (G2G3), of gelsolin was used (Fig. 4*B*). The wild-type G2G3 remained intact, whereas the mutants were completely cleaved, and the nanobody afforded almost complete protection against cleavage.

We hypothesized that the interaction between domains G2 and G3 may be important in protecting G2 from cleavage. To test this hypothesis, we created mutations in G3 that would be predicted to disrupt the active structure of G2G3 (*SI Appendix*, Fig. S2). These mutants were subjected to the furin cleavage assay (Fig. 4*C*). All 3 non-FAF mutants (K314M, L361D, and Q364L) were able to induce susceptibility to furin cleavage, and total protection from furin cleavage was imparted by the inclusion of the nanobody, despite it binding to the other domain (G2) rather than to the domain with mutation sites (G3) (Fig. 4*D*).

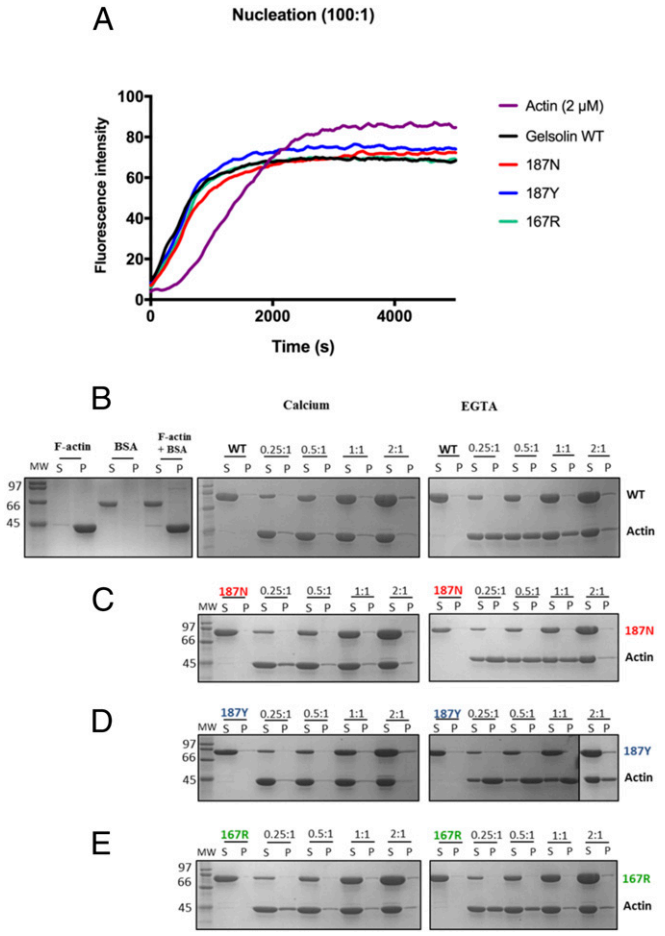

Fig. 2. FAF gelsolin activity at pH 6.5. (*A*) Actin nucleation assay with FAF gelsolin mutants. G-actin was incubated with different gelsolin mutants at a molar ratio of 1:100 for 1 h followed by the addition of 10× KMEI buffer. FAF mutants nucleate actin filaments similarly as wild-type gelsolin. Data represent the average of 3 experiments. (*B*–*E*) FAF gelsolins sever F-actin. Sedimentation assays of FAF gelsolin were carried out under EGTA and calcium conditions. F-actin was incubated with different concentrations of wild-type and mutant gelsolins for 1 h at room temperature and subjected to ultracentrifugation, and the supernatants (*S*) and pellets (*P*) were analyzed by SDS/PAGE. (*B*) WT, (*C*) 187N, (*D*) 187Y, (*E*) 167R. *Right*, 1.5 mM EGTA. *Left*, 1 mM calcium chloride.

To understand the impact of these mutations on the gelsolin structure, we performed molecular dynamics (MD) simulations for the wild type, the FAF mutant, and the non-FAF G2G3 mutants. All of the mutations tend to disrupt the G2G3 structure as indicated by the increase of the overall root-mean-square deviation (RMSD) from the starting structures and the center of mass (COM) distances between the 2 domains (Fig. 5 and *SI Appendix*, Figs. S5–S7). The structure disruption effect can also be observed from the potentials of mean force, which show that the free-energy penalties of separating the domains G2 and G3 are significantly reduced in all of the mutants (Fig. 5*B* and *SI Appendix*, Fig. S5*B*). More detailed analysis suggests that the mutations mainly disrupt the G2-G3 interface, and the structures of the individual domains mostly remain intact through the timescale

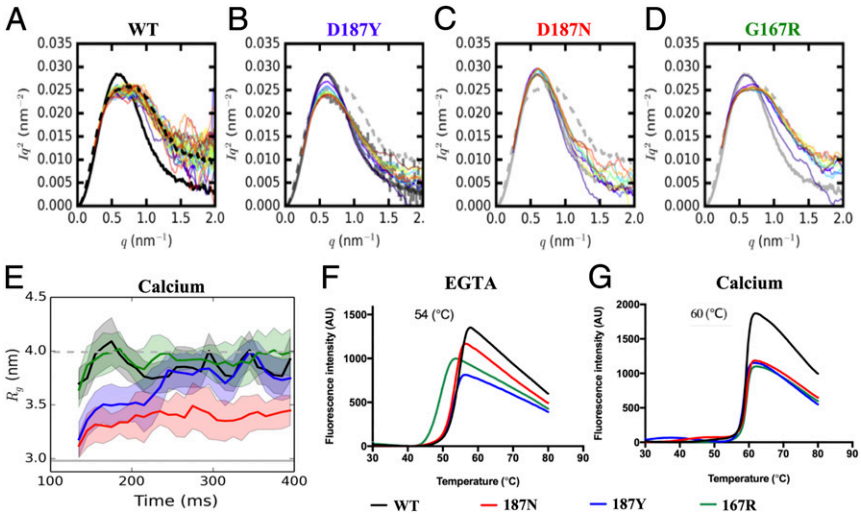

Fig. 3. Kratky plots of the time points of calcium activation of (*A*) WT, (*B*) D187Y, (*C*) D187N, and (*D*) G167R gelsolins. In all panels, the individual frames of the stopped-flow experiments, with 4 mg/mL protein in the presence of 1 mM Ca^{2+} are shown color-coded from blue (130 ms) to red (400 ms) for increasing time points. For the WT gelsolin, steady state continuous flow plots are included, EGTA (solid black line) and calcium (dashed black line). For reference, these WT continuous flow profiles are also shown as gray lines in the mutant panels. (*E*) Time dependence of Rg values. (*F* and *G*) Thermal shift assays. Thermal denaturation studies of WT and mutants in the presence of EGTA (*F*) or calcium chloride (*G*). Values of the midpoints of the WT thermal denaturation profiles are indicated.

(150 ns) of the simulations (*SI Appendix*, Figs. S8 and S9). The above observations are consistent with the results of the furin cleavage assay, since G3 covers the furin-cleavage site on G2 in the calcium-bound conformation (21), and the disruption of the G2-G3 interface by mutation makes the site accessible to furin.

Discussion

We have probed the effect of FAF mutations on the structure and activity of full-length gelsolin. The FAF mutations have minimal impact on the structure of gelsolin and have little consequence on its activity. The calcium-binding site mutations delay calcium-induced activation, while the G167R mutation destabilizes the inactive conformation. Removal of domains G1 and G4-G6 results in a fragment of gelsolin (G2G3) that is sensitized to furin cleavage. This suggests that the removed domains contribute to the stability of G2 and impart partial protection from cleavage by furin to the FAF mutant gelsolins. Similarly, binding of a nanobody to G2, to a distant site to the furin-cleavage site, also engenders protection. These data all point toward the conformation of G2 to be close to the limits of stability (19, 32). A second factor in determining susceptibility to cleavage is the accessibility of the furin cleavage site. Loss of interactions with residue 187 or introduction of a steric handicap (G167R) lead to the domain sampling of conformations that can be cleaved by furin. In calcium-bound G2G3 this site on G2 is occluded by G3. The non-FAF mutants demonstrated that disruption of this interface results in increased cleavage. Dissociation of G3 will simultaneously have an impact on the stability of G2, due to the loss of this stabilizing interaction. Inspection of the activated structure of G1-G3 reveals that each of the FAF mutations in domain 2 (G167R, N184K, and D187N/Y) will directly impact the ability for G3 to cover the FAF-cleavage site on G2 (27). D187N/Y mutants disrupt the calcium-binding site, which holds the G2-G3 linker in place, while G167R and N184K point their sidechains at the G2-G3 linker, likely perturbing the positioning of the linker and destabilizing the G2:G3 interaction. We note that the P432R and A551P mutation sites lie at positions in both the calcium-free and calcium-bound conformations of gelsolin that may be expected to disrupt the G4:G5 interface. Thus, these mutants may disrupt the general structure of gelsolin, and since G3 is linked to G4, any disruption to the G4:G5 may have knock-on effects for the dynamics of the G2:G3 interaction and sensitize G2 to cleavage. We conclude that G2 is quasi-stable, and any perturbation that decreases the stability of G2 and disrupts the G2:G3 interaction leads to exposure of the furin cleavage site, resulting in the fragmentation of the protein. This mechanism predicts that there are further mutations to gelsolin, such as the non-FAF mutants created here, that can increase the susceptibility of the gelsolin to cleavage by furin. Should such variants be present in the human population, then the mechanism also predicts that these mutant gelsolins will be cleaved in the trans-Golgi, and that the carriers may exhibit FAF symptoms, following further extracellular cleavage and self-assembly of the resultant peptides into fibrils.

Materials and Methods

Constructs and Protein Production. DNA encoding full-length human gelsolin (residues 25–755) and G2-G3 (residues 132–372) was engineered into the expression vector pSY5, a modified version of pET-21d(+) (Novagen), which places an N-terminal, 8-histidine tag, followed by a human rhinovirus 3C protease cleavage site ahead of the N termini of the proteins. Mutated variants of full-length gelsolin (D187N/Y and G167R) were constructed by using QuikChange site-directed mutagenesis (Stratagene) with the full-length wild-type gelsolin and G2-G3 as the templates. DNA sequencing verified the identities of the constructs. Recombinant proteins were expressed and purified as described previously (27). The oligomeric states of the full-length proteins were analyzed by size exclusion chromatography (SEC) monitored by UV absorption and multiangle light scattering (MALS), which gave profiles consistent with monomeric proteins with estimated molecular weights between 67–80 kDa for these 83-kDa proteins (*SI Appendix*, Fig. S10). Nanobody Nb11 was purified as previously reported (32).

Size Exclusion Chromatography–Multiangle Light Scattering. DAWN HELEOS 8 multiangle light-scattering 3-angle (43.6°, 90°, and 136.4°) detector and a 663-nm laser beam, with a Wyatt QELS dynamic light-scattering module for determination of molecular size and an Optilab T-rEX refractometer, were used after size exclusion chromatography (Superdex 200 10/300 GL, GE Healthcare). Experiments were performed using an ÄKTA explorer system (GE Healthcare). All experiments were performed at room temperature (25 °C). Data collection and SEC-MALS analysis were performed with ASTRA 6.1 software (Wyatt Technology). The refractive index of the solvent was defined as 1.331, and the viscosity was defined as 0.8945 cP. The dn/dc (refractive index increment) value for all samples was defined as 0.185 mL/g. For SEC-MALS experiments, 100 μL of 10 mg/mL gelsolin proteins were loaded on a Superdex 200 column with running buffer of 50 mM Tris·HCl, pH 7.4, and 150 mM NaCl.

Crystallization and Data Collection. Crystals of Ca-free GFL mutants (D187N, D187Y, and G167R) were obtained after mixing 18 mg/mL solution of protein with precipitant solution (15% glycerol, 1.5 M ammonium sulfate, and 0.1 M Tris·HCl, pH 8.5) at 25 °C by using the hanging-drop vapor diffusion method. The crystals were frozen in liquid nitrogen after soaking in the precipitant solution supplemented with 20% glycerol. X-ray diffraction data were collected on beamline BL13B1 on an Area Detection Systems Corporation Quantum-315 CCD detector at the National Synchrotron Research Center (Hsinchu, Taiwan). The wavelength was set to 1 Å, and the data were collected at 105 K. D187N mutant data were collected on beamline I02 on

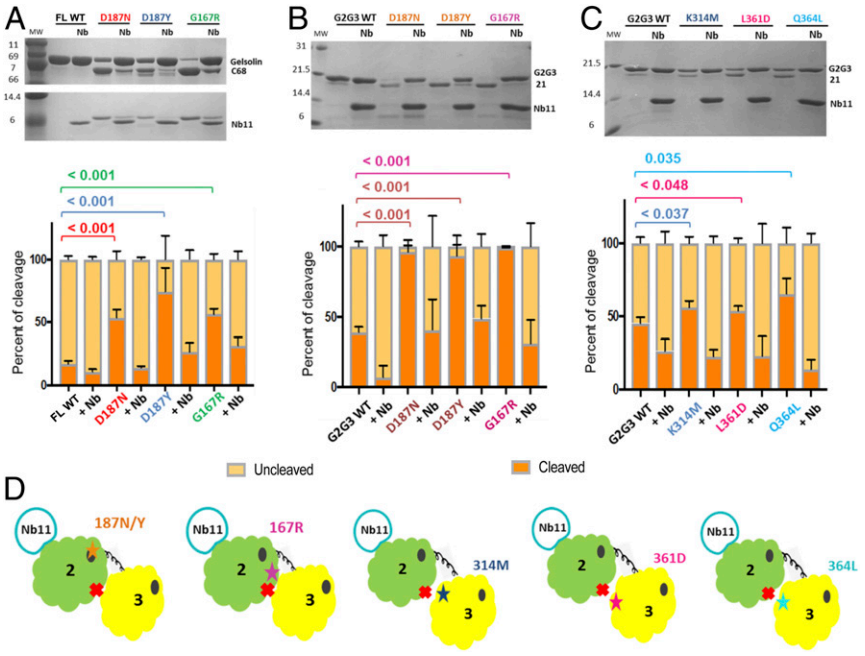

Fig. 4. Gelsolin FAF mutants are protected by Nb11 from furin cleavage. Susceptibility to furin cleavage was tested in vitro for both full-length (FL) and G2G3 constructs and analyzed by SDS/PAGE. Incubation of the (*A*) FL mutants and (*B*) G2G3 mutants with furin for 3 h. Production of cleaved fragments is observed for the mutants, which is more efficient for G2G3 than FL under the same conditions. Inclusion of Nb11 inhibits the furin cleavage in *A* and *B*. "Nb" refers to the inclusion of nanobody. Below, the extent of cleavage was assessed by densitometry as the average value from three gels. (*C*) Furin cleavage was tested for the non-FAF G2G3 mutants, which show a cleaved gel band assessed after 3 h. Inclusion of Nb11 inhibited the appearance of this gel band. Time course and titrations for the furin assay are found in *SI Appendix*, Figs. S3 and S4. Statistical tests were applied on differences observed in the percentage of cleaved proteins. Data are the average of three independent experiments ±SD. Student's *t* test (2-sided) was used for statistical analysis. (*D*) Cartoons indicate the relative positions of the mutation sites (stars) relative to G2 (green), G3 (yellow), the cleavage site (red cross), calcium-binding sites (black ovals), and the Nb11-binding site.

Pilatus 6MF detector at the Diamond Light Source. Data were indexed, integrated, and scaled using HKL2000 (33) or xia2 (34). Crystal structures were solved by molecular replacement using human Ca-free gelsolin as the search model (PDB 3FFN) (27, 35). The structures were refined using REFMAC5 (36) or Phaser (35). Manual building was made using the graphics program COOT (37). Data collection and refinement statistics are shown in *SI Appendix*, Table S1.

Actin Nucleation Assay. Ten percent pyrene-labeled G-actin (2 μM) was incubated with the respective gelsolin protein at a molar ratio of 1:100 in buffer A (2 mM Tris·HCl, pH 8, 0.2 mM ATP, 0.1 mM $CaCl_2$, 0.5 mM DTT, 1 mM Na azide) in a final volume of 90 μL for 30 min in 96-well black flat-bottomed plates (Corning). Ten microliters of 10× polymerization buffer (500 mM KCl, 10 mM $MgCl_2$, 10 mM EGTA (ethylene glycol-bis(β-aminoethyl ether)-*N,N,N′,N′*-tetraacetic acid), 100 mM imidazole HCl, pH 7) was added to each reaction before measurement of the fluorescence intensity at excitation and emission wavelengths of 365 and 407 nm, respectively, with a Safire^2 fluorimeter (TECAN).

Thermal Shift Assays. The reaction mixture, consisting of 12.5 μL of (20 mM Hepes, 100 mM NaCl, pH 6.5) buffer with either 1 mM $CaCl_2$ or 1 mM EGTA, 5 μL of 2.5 mg/mL protein, and 7.5 μL of 100× Sypro orange (Molecular Probes), was added to each well in 96-well PCR plates (BioRad). Plates were sealed and heated with a temperature range from 20 °C to 80 °C in 0.2 °C increments in an iCycler iQ Real-Time PCR Detection System (BioRad). The transition temperature of each protein was determined as described previously (38).

Furin Assays. Gelsolin (5 mM) was incubated at 37 °C with 1 unit of furin (New England Biolabs) in 20 mM MES (2-(*N*-morpholino)ethanesulfonic acid) pH 6.5, 100 mM NaCl, 1 mM $CaCl_2$. After 60 min incubation, reactions were quenched by the addition of EGTA (100 mM) on ice. The proteolysis reaction was monitored by SDS/PAGE. The extent of cleavage was assessed by densitometry as the average value from 3 gels.

Actin Sedimentation Assay. Gelsolin WT and mutants were tested for their ability to bind F-actin under both calcium and EGTA conditions. Various concentrations of the protein were incubated with F-actin in 50 μL of polymerization buffer for 30 min before centrifugation for 1 h at 150,000 × *g* using a TLA120.1 rotor in a Beckman Optima Max ultracentrifuge. Fifteen microliters of each sample (supernatant and pellet) were analyzed by SDS/PAGE.

SAXS Data Acquisition. SAXS data on gelsolin WT and three mutants; D187N, D187Y, and G167R were collected on beamline ID02 at the European Synchrotron Research Facility (ESRF). The wavelength was set to $\lambda = 1$ Å, and the sample-to-detector (Pilatus 300K) distance was set to either 1.2 or 2.5 m. The proteins at 8 mg/mL in 50 mM MES, pH 6.5, 150 mM NaCl, 1 mM EGTA were mixed with an equal volume of 50 mM MES, pH 6.5, 150 mM NaCl, 2 mM $CaCl_2$ using a stopped flow device (BioLogic, SFM-400). The mixing volume was 0.1 mL, and the mixing time was 95 ms, after which 30 images were recorded at 10 ms per frame. Each experiment was repeated at least 3 times, as were the matched buffer experiments used for background subtraction. This protocol was adopted to collect different time frames during the protein activation. To get a more accurate estimation of the parameters for the starting (EGTA) and ending (calcium) states for the WT protein, a second set of exposures, in which the proteins were preequilibrated (30 min) in their final buffer conditions

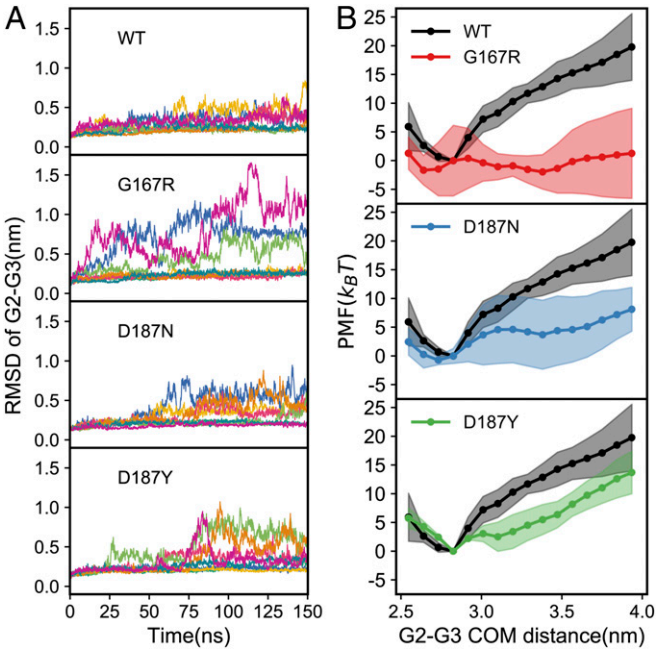

Fig. 5. Molecular dynamics simulations of the WT and FAF mutants. (*A*) RMSD of G2G3 relative to the native structure of the calcium-bound active conformation (PDB 3FFK) as a function of simulation time. (*B*) Potential of mean force as a function of COM distance. The PMF profiles and the errors were calculated by the averages and SDs of the results from 3 independent umbrella-sampling simulations.

before being exposed in the continuous flow mode (30 images recorded at 10 ms per frame) and the images averaged together. The final concentrations of all protein samples were 4 mg/mL in the presence of 1 mM Ca^{2+}.

SAXS Data Analysis. For each sample, SAXS snapshots were averaged, then buffer subtracted. SAXS data were analyzed using the ATSAS 2.7.2 software. To avoid spurious scattering from the beam stop, a minimum threshold of the scattering angle $q = 0.15$ nm^{-1} was used. Before data fitting, time-resolved measurements at each time point were averaged across experimental replicates, while flow-through experiments were averaged across 30 successive frames. For all flow-through experiments, the *autorg* command was used to automatically determine Rg by Guinier fitting (39). Because the time-resolved measurements are noisier, manual Guinier fitting was performed with the PRIMUS graphical user interface (GUI) (40). In all cases, the number of data points used in the Guinier fit were constrained such that $qRg \leq 1.3$. Indirect Fourier Transform fits were also performed manually (by varying Dmax—the maximum dimension—and the regularization parameter) using the PRIMUS GUI. Due to lower signal-to-noise at higher q, only data less than 2 nm^{-1} were used for all indirect Fourier Transform fits.

MD Simulations. All-atom MD simulations were performed on the wild-type G2G3 and its 6 mutants. The initial structure of the wild-type G2G3 was extracted from the crystal structure of the active conformation of the gelsolin (PDB 3FFK) (27). The sidechains of the 6 mutants were replaced by using the software Modeller9 (41). All simulations were carried out using Gromacs 5.1.4 (42) with the CHARMM27 force field for protein and the SPC/E model for water molecules (43). Cl^- and Na^+ were added to neutralize the system and to produce the physiological salt concentration (150 mM). Eight independent simulations with different initial velocities were conducted for each of the systems. The final simulations were performed in the NPT ensemble at 300 K and 1 atm with the integration time step of 2 fs. For better characterization of the stability changes caused by the mutations, we also calculated the potential of mean force (PMFs) along the separation of the 2 domains for the wild-type G2G3 and its mutants by using umbrella-sampling simulations (44) and the MBAR reweighting algorithm (45). Fifteen harmonic umbrella potentials were placed along the distances between the centers of mass of the 2 domains ranging from 25.2 Å to 39.2 Å with the force constant of 20 kJ/mol/$Å^2$. Each umbrella window was simulated for 20 ns, with the first 10 ns omitted in the PMF calculations. We repeated the umbrella-sampling simulations 3 times with different initial structures in the umbrella windows to estimate the errors of the PMFs arising from sampling.

ACKNOWLEDGMENTS. We thank Agency for Science, Technology and Research (A*STAR) for support and are grateful for the technical services provided by the National Synchrotron Radiation Research Center (Taiwan), Diamond Light Source (UK), and The European Synchrotron Radiation Facility (France).

1. G. Boysen, G. Galassi, Z. Kamieniecka, J. Schlaeger, W. Trojaborg, Familial amyloidosis with cranial neuropathy and corneal lattice dystrophy. *J. Neurol. Neurosurg. Psychiatry* **42**, 1020–1030 (1979).
2. S. Kiuru, E. Matikainen, M. Kupari, M. Haltia, J. Palo, Autonomic nervous system and cardiac involvement in familial amyloidosis, Finnish type (FAF). *J. Neurol. Sci.* **126**, 40–48 (1994).
3. C. P. Maury, J. Kere, R. Tolvanen, A. de la Chapelle, Homozygosity for the Asn187 gelsolin mutation in Finnish-type familial amyloidosis is associated with severe renal disease. *Genomics* **13**, 902–903 (1992).
4. J. Meretoja, Familial systemic paramyloidosis with lattice dystrophy of the cornea, progressive cranial neuropathy, skin changes and various internal symptoms. A previously unrecognized heritable syndrome. *Ann. Clin. Res.* **1**, 314–324 (1969).
5. M. Taira *et al*., Clinical features and haplotype analysis of newly identified Japanese patients with gelsolin-related familial amyloidosis of Finnish type. *Neurogenetics* **13**, 237–243 (2012).
6. K. J. Park *et al*., The first Korean family with hereditary gelsolin amyloidosis caused by p.D214Y mutation in the GSN gene. *Ann. Lab. Med.* **36**, 259–262 (2016).
7. B. V. Maramattom, Y. T. Chickabasaviah, A new Indian family affected by gelsolin amyloidosis. *Neurol. India* **61**, 673–675 (2013).
8. F. Lucero Saá, F. A. Cremona, N. X. Mínguez, M. L. Igarzabal, P. Chiaradía, The first Argentinian family with familial amyloidosis of the Finnish type. *Case Rep. Ophthalmol.* **8**, 446–451 (2017).
9. I. Conceição *et al*., Gelsolin-related familial amyloidosis, Finnish type, in a Portuguese family: Clinical and neurophysiological studies. *Muscle Nerve* **28**, 715–721 (2003).
10. H. P. Solari, M. P. Ventura, E. Antecka, R. Belfort Junior, M. N. Burnier, Jr, Danish type gelsolin-related amyloidosis in a Brazilian family: Case reports. *Arq. Bras. Oftalmol.* **74**, 286–288 (2011).
11. X. Feng, H. Zhu, T. Zhao, Y. Hou, J. Liu, A new heterozygous G duplicate in exon1 (c.100dupG) of gelsolin gene causes Finnish gelsolin amyloidosis in a Chinese family. *Brain Behav.* **8**, e01151 (2018).
12. A. de la Chapelle *et al*., Gelsolin-derived familial amyloidosis caused by asparagine or tyrosine substitution for aspartic acid at residue 187. *Nat. Genet.* **2**, 157–160 (1992).
13. S. Sethi *et al*., Renal amyloidosis associated with a novel sequence variant of gelsolin. *Am. J. Kidney Dis.* **61**, 161–166 (2013).
14. Y. A. Efebera *et al*., Novel gelsolin variant as the cause of nephrotic syndrome and renal amyloidosis in a large kindred. *Amyloid* **21**, 110–112 (2014).
15. K. Z. Oregel *et al*., Atypical presentation of gelsolin amyloidosis in a man of African descent with a novel mutation in the gelsolin gene. *Am. J. Case Rep.* **19**, 374–381 (2018).
16. M. Sridharan *et al*., A patient with hereditary ATTR and a novel AGel p.Ala578Pro amyloidosis. *Mayo Clin. Proc.* **93**, 1678–1682 (2018).
17. S. Sethi *et al*., Clinical, biopsy, and mass spectrometry findings of renal gelsolin amyloidosis. *Kidney Int.* **91**, 964–971 (2017).
18. S. L. Kazmirski *et al*., Loss of a metal-binding site in gelsolin leads to familial amyloidosis-Finnish type. *Nat. Struct. Biol.* **9**, 112–116 (2002).
19. T. Giorgino *et al*., Nanobody interaction unveils structure, dynamics and proteotoxicity of the Finnish-type amyloidogenic gelsolin variant. *Biochim. Biophys. Acta Mol. Basis Dis.* **1865**, 648–660 (2019).
20. C. D. Chen *et al*., Furin initiates gelsolin familial amyloidosis in the Golgi through a defect in Ca(2+) stabilization. *EMBO J.* **20**, 6277–6287 (2001).
21. L. D. Burtnick, D. Urosev, E. Irobi, K. Narayan, R. C. Robinson, Structure of the N-terminal half of gelsolin bound to actin: Roles in severing, apoptosis and FAF. *EMBO J.* **23**, 2713–2722 (2004).
22. R. C. Robinson, S. Choe, L. D. Burtnick, The disintegration of a molecule: The role of gelsolin in FAF, familial amyloidosis (Finnish type). *Proc. Natl. Acad. Sci. U.S.A.* **98**, 2117–2118 (2001).
23. A. Srivastava *et al*., The gelsolin pathogenic D187N mutant exhibits altered conformational stability and forms amyloidogenic oligomers. *Biochemistry* **57**, 2359–2372 (2018).
24. F. Bonì *et al*., Gelsolin pathogenic Gly167Arg mutation promotes domain-swap dimerization of the protein. *Hum. Mol. Genet.* **27**, 53–65 (2018).
25. J. P. Solomon, L. J. Page, W. E. Balch, J. W. Kelly, Gelsolin amyloidosis: Genetics, biochemistry, pathology and possible strategies for therapeutic intervention. *Crit. Rev. Biochem. Mol. Biol.* **47**, 282–296 (2012).
26. L. J. Page *et al*., Metalloendoprotease cleavage triggers gelsolin amyloidogenesis. *EMBO J.* **24**, 4124–4132 (2005).
27. S. Nag *et al*., Ca2+ binding by domain 2 plays a critical role in the activation and stabilization of gelsolin. *Proc. Natl. Acad. Sci. U.S.A.* **106**, 13713–13718 (2009).
28. H. Zorgati *et al*., Crystal structure of calcium free human gelsolin amyloid mutant G167R. Protein Data Bank. https://www.rcsb.org/structure/6jeg. Deposited 5 February 2019.
29. H. Zorgati *et al*., Crystal structure of calcium free human gelsolin amyloid mutant D187N. Protein Data Bank. https://www.rcsb.org/structure/6jco. Deposited 29 January 2019.
30. H. Zorgati *et al*., Crystal structure of calcium free human gelsolin amyloid mutant D187Y. Protein Data Bank. https://www.rcsb.org/structure/6jeh. Deposited 5 February 2019.
31. H. Choe *et al*., The calcium activation of gelsolin: Insights from the 3A structure of the G4-G6/actin complex. *J. Mol. Biol.* **324**, 691–702 (2002).
32. W. Van Overbeke *et al*., An ER-directed gelsolin nanobody targets the first step in amyloid formation in a gelsolin amyloidosis mouse model. *Hum. Mol. Genet.* **24**, 2492–2507 (2015).
33. Z. Otwinowski, W. Minor, Processing of X-ray diffraction data collected in oscillation mode. *Methods Enzymol.* **276**, 307–326 (1997).
34. G. Winter, C. M. Lobley, S. M. Prince, Decision making in xia2. *Acta Crystallogr. D Biol. Crystallogr.* **69**, 1260–1273 (2013).
35. P. D. Adams *et al*., PHENIX: A comprehensive Python-based system for macromolecular structure solution. *Acta Crystallogr. D Biol. Crystallogr.* **66**, 213–221 (2010).
36. G. N. Murshudov, A. A. Vagin, E. J. Dodson, Refinement of macromolecular structures by the maximum-likelihood method. *Acta Crystallogr. D Biol. Crystallogr.* **53**, 240–255 (1997).
37. P. Emsley, B. Lohkamp, W. G. Scott, K. Cowtan, Features and development of Coot. *Acta Crystallogr. D Biol. Crystallogr.* **66**, 486–501 (2010).
38. M. W. Pantoliano *et al*., High-density miniaturized thermal shift assays as a general strategy for drug discovery. *J. Biomol. Screen* **6**, 429–440 (2001).
39. M. V. Petoukhov, D. I. Svergun, Analysis of X-ray and neutron scattering from biomacromolecular solutions. *Curr. Opin. Struct. Biol.* **17**, 562–571 (2007).
40. P. V. Konarev, V. V. Volkov, A. V. Sokolova, M. H. J. Koch, D. I. Svergun, PRIMUS: A Windows PC-based system for small-angle scattering data analysis. *J. Appl. Cryst.* **36**, 1277–1282 (2003).
41. A. Sali, T. L. Blundell, Comparative protein modelling by satisfaction of spatial restraints. *J. Mol. Biol.* **234**, 779–815 (1993).
42. M. J. Abraham *et al*., GROMACS: High performance molecular simulations through multi-level parallelism from laptops to supercomputers. *SoftwareX* **1–2**, 19–25 (2015).
43. A. D. MacKerell *et al*., All-atom empirical potential for molecular modeling and dynamics studies of proteins. *J. Phys. Chem. B* **102**, 3586–3616 (1998).
44. G. M. Torrie, J. P. Valleau, Nonphysical sampling distributions in Monte Carlo free-energy estimation: Umbrella sampling. *J. Comput. Phys.* **23**, 187–199 (1977).
45. M. R. Shirts, J. D. Chodera, Statistically optimal analysis of samples from multiple equilibrium states. *J. Chem. Phys.* **129**, 124105 (2008).